ACS OMEGA

Open Access

http://pubs.acs.org/journal/acsodf

Article

Comparative Study on Flow Characteristics in Deep Marine and Marine−Continental Transitional Shale in the Southeastern Sichuan Basin, China

Liangliang Liu, Jing Li,* Shixin Zhou, Gengrong Chen, Yaoyu Li, Wenjun Pang, and Hao Wang

Cite This: *ACS Omega* 2024, 9, 22016−22030

Read Online

ACCESS | Metrics & More | Article Recommendations

ABSTRACT: Permeability is a significant characteristic of porous media and a crucial parameter for shale gas development. This study focuses on deep marine and marine−continental transitional shale in the southeastern Sichuan area using the gas pulse decay testing method to systematically analyze the gas permeability, stress sensitivity, and gas transport mechanisms of shale under different pressure conditions and directions. The results show that the porosity and gas permeability of the deep marine shale are greater compared to those of the marine−continental transitional shale. The elevated fluid pressure in the deep marine shale offers superior conditions for the preservation of nanopores, while the high quartz content provides advantageous conditions for fluid transport in nanopore channels. The permeability and stress sensitivity of the deep marine shale are greater than those of the marine−continental transitional shale, and the stress sensitivity is greater in the perpendicular bedding direction than in the parallel bedding direction, possibly related to the mineral composition of shale and the compaction it has undergone. The flow mechanism of the deep marine shale is transition flow and Knudsen flow, while that of the marine−continental transitional shale is transition flow. The deep marine shale possesses smaller nanopore sizes and a higher quantity of micropores, which create advantageous conditions for gas transport within nanopores. During the process of extracting shale gas, the extraction of gas causes a decrease in pore pressure and an increase in effective stress, resulting in a reduction in permeability. However, when the pore pressure reaches a specific value, the enhanced slippage effect leads to an increase in permeability, which is advantageous for gas extraction. In the later stage of shale gas well production, intermittent production plans can be developed considering the strength of the slippage effect, leading to a significant improvement in production efficiency.

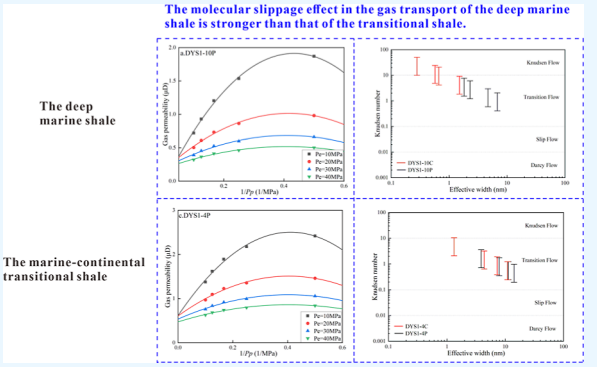

1. INTRODUCTION

China is currently confronted with the dual challenges of environmental pollution and energy shortages. These challenges arise from the rising demand for oil and gas resources coupled with the diminishing reserves of conventional oil and gas. Optimizing energy structure is one of the important ways to alleviate environmental pressure,[1] and increasing efforts to develop clean energy such as natural gas is the main method for China to address this issue. Shale gas is a vast unconventional natural gas resource worldwide, characterized by long extraction life, stable extraction, significant development potential, and high commercial value. The "shale gas revolution" in the United States has shifted the country from a major importer to an exporter of natural gas and has also triggered a global boom in shale gas exploration, development, and research. Currently, countries such as the United States, Canada, and China have successfully achieved commercial production of shale gas. Among them, the United States has made significant progress by attaining large-scale commercial production and entering a phase of rapid development in shale gas exploration and production.[2]

According to incomplete statistics, the remaining recoverable reserves of shale gas in China are estimated to be 3.39×10^{14} m^3, which is equivalent to 15% of the total global shale gas reserves.[3] In 2022, the production of shale gas reached 240×10^8 m^3.[4] Through more than a decade of exploration and development efforts, significant progress has been made in the effective development of marine shale gas resources in the Sichuan Basin and its adjacent areas.[5,6] The Ordovician Wufeng Formation and the Silurian Longmaxi Formation have become the main target formations of shale gas exploration and development in the

Received: December 28, 2023
Revised: April 22, 2024
Accepted: April 25, 2024
Published: May 8, 2024

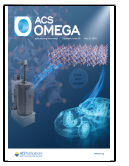

Sichuan Basin. Several shale gas production areas, including Fuling, Weirong, Weiyuan−Changning, and Luzhou−Yuxi, have been successively established one after another. The cumulative proven geological reserves of shale gas in this region amount to 2.81×10^{12} m^3. In 2022, shale gas production in the Sichuan Basin reached approximately 223.23×10^8 m^3, accounting for 93% of the total shale gas production and 10% of China's total natural gas production (2201.1×10^8 m^3). Except for the Ordovician Wufeng Formation and the Silurian Longmaxi Formation, shale gas exploration and evaluation in other formations within the Sichuan Basin are still in progress. Meanwhile, the region possesses abundant marine−continental transitional shale gas resources with significant exploration potential.[1,7−9] However, due to the delayed initiation of research and the relatively low level of exploration and development, scale development has not been achieved yet.[10]

In the past decade, significant progress has been made in the exploration and development of shale gas, leading to successful commercial exploitation in China. However. there has been no significant breakthrough in the research on the fundamental theory of shale gas. Numerous pressing issues still need to be solved.[11−14] Shale formations are characterized by low porosity and low permeability, and only a limited number of shale gas wells with highly developed natural fractures can directly produce natural gas under natural completion conditions.[15−17] Consequently, hydraulic fracturing technology is necessary for the majority of shale gas wells to modify the shale reservoir and enhance its permeability, enabling the production of natural gas. During production, gas from the shale reservoir flows successively through the shale matrix, the fractures created by hydraulic fracturing, and ultimately reaches the wellbore of the production well. The permeability of the shale matrix signifies the fluid transport capacity within its pore media, serving as a crucial characteristic for shale gas exploration and development.[11,18,19]

Permeability is a measure of a rock's ability to allow fluid flow under specific pressure conditions. Theoretically, the permeability of rock only reflects the inherent characteristics of the rock and is independent of the fluid properties and measurement conditions. It is often referred to as intrinsic permeability or liquid permeability. However, practical measurements have shown that the permeability obtained under the same conditions for the same rock sample varies when using different gases. The permeability measured using gas is referred to as apparent permeability or gas permeability, which typically exceeds the intrinsic permeability. The complex pore structure and stress sensitivity of shale pose challenges in predicting the in situ intrinsic permeability, which is crucial for evaluating shale gas resources.[13,20,21]

The apparent permeability in low-permeability porous media is often affected by the molecular slippage effect, making it unsuitable for direct stress sensitivity evaluation. Typically, the apparent permeability needs to be corrected using the Klinkenberg correction to determine the intrinsic permeability for stress sensitivity evaluation.[22] The slippage effect refers to a molecular transport mechanism observed in nonviscous fluids, which depends on the relative size between the mean free path of gas molecules and the flow aperture. The molecular slippage effect may cause the apparent gas permeability to deviate from Darcy's law, as it is not solely controlled by the gas pressure gradient. This, in turn, affects the gas transport mechanism in shale.[23−25] Currently, there is insufficient research on the gas flow mechanisms in low-permeability porous media, which are predominantly influenced by the molecular slippage effect. However. the quantitative characterization of the contribution of the molecular slippage effect has always been a challenging issue in the research.[26]

Two commonly used testing methods for determining apparent permeability are a steady-state method and an unsteady-state method. The steady-state method involves measuring the gas flow through the rock core and then calculating the permeability according to Darcy's law. For low-permeability porous media, the system requires a significant amount of time to reach equilibrium, resulting in prolonged experimental durations and increased susceptibility of experimental results to environmental temperature. Consequently, this leads to poor repeatability.[27−30] The unsteady-state method, also referred to as the pressure pulse decay method, is currently the most effective method for measuring permeability in low-permeability porous media, particularly in shale formations. It is widely employed in the investigation of permeability in mudstone and tight sandstone. One of the primary advantages of this method is its short testing duration, which is particularly beneficial for porous media with permeability less than 1 μD, such as shale and sandy mudstone.[14,31−36]

Shale is a typical multiscale porous medium containing artificial hydraulic fractures, natural fractures, micropores, and nanopores. The gas occurrence modes and transport mechanisms in shale vary at different scales.[37,38] The gas transport processes in shale gas development mainly include the following: (1) free gas in artificial hydraulic fractures and natural fractures flows into the wellbore through Darcy flow; (2) free gas in pores flows into the low-pressure region through continuous flow, slip flow, and transition flow in the fracture network system; (3) desorption of gas adsorbed on pore walls replenishes free gas in pores, and gas also enters the fracture network system through surface diffusion; and (4) gas dissolved in kerogen increases the amount of gas adsorbed on pore walls through configurational diffusion, indirectly increasing shale gas production. Nanopore gas transport is a crucial aspect of shale gas development; therefore, understanding the nanopore gas transport mechanisms and conducting transport simulations are key technologies for efficient shale gas development.[39,40]

The marine shale of the Ordovician Wufeng Formation and the Silurian Longmaxi Formation in the southeastern Sichuan Basin has proven to be a highly productive shale formation for shale gas exploration and development in China.[41,42] The Permian Longtan Formation, a marine−continental transitional shale, exhibits several favorable geological characteristics for shale gas formation, including the development of organic-rich mud shale, high porosity, and high organic carbon content, which possesses favorable geological conditions for shale gas formation and has significant potential for shale gas exploration.[43−45] In this study, the stress pulse decay method is employed to determine the apparent permeability values of the Longmaxi Formation marine shale and Longtan Formation marine−continental transitional shale in the southeastern Sichuan area under different sample depths, confining pressures, and pore pressure conditions. The effective stress coefficients were calculated based on response surface model fitting, the intrinsic permeability was obtained to analyze its stress sensitivity with Klinkenberg correction, the relative contribution of molecular slippage effect in apparent permeability under different stress conditions was quantified, the gas transport mechanisms in shales with different stratigraphic positions were

https://doi.org/10.1021/acsomega.3c10441
ACS Omega 2024, 9, 22016−22030

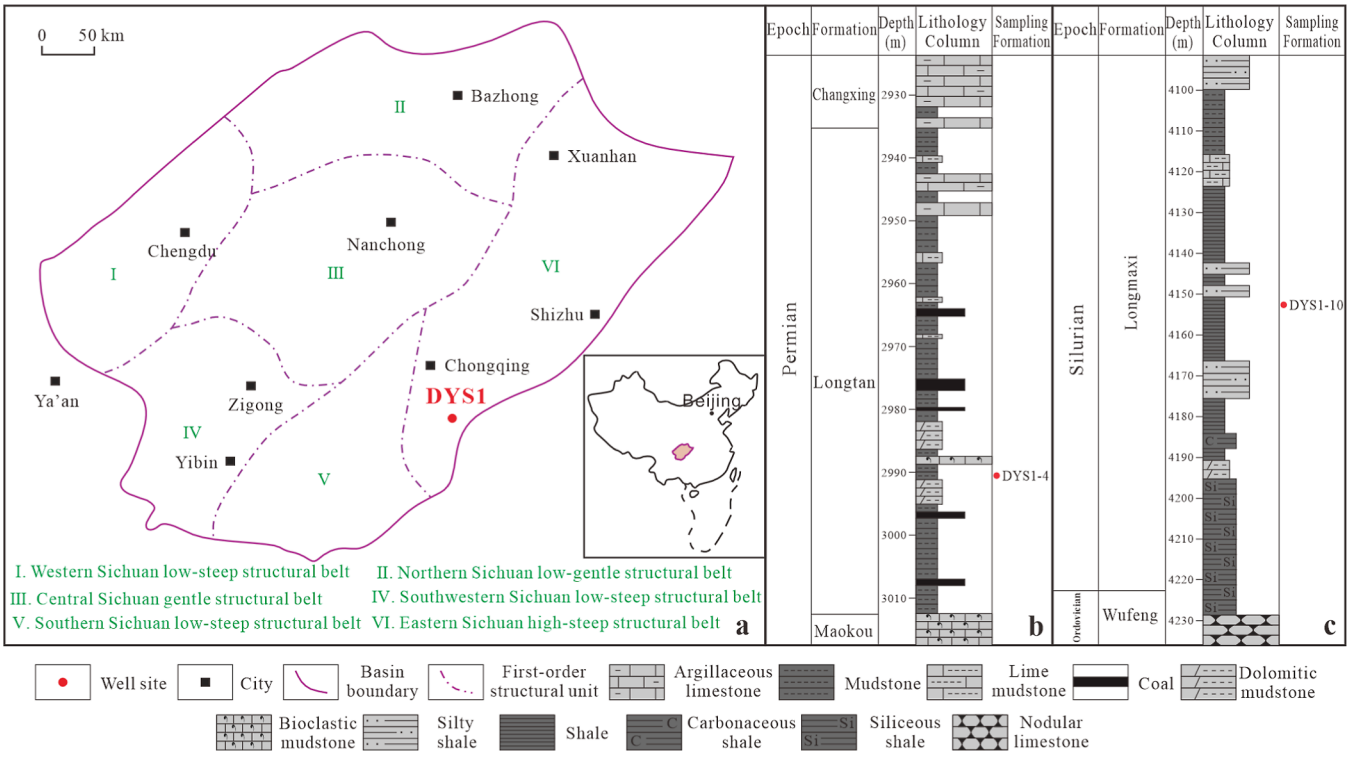

Figure 1. Sampling location and stratigraphic section. (a) Sampling location. (b) Sampling stratigraphic section for transitional shale. (c) Sampling stratigraphic section for marine shale.

Table 1. Mineral Content of Experimental Samples

sample	depth (m)	TOC (%)	quartz	clay	feldspar	calcite	dolomite	pyrite	others
DYS1−4	2991.30	1.23	30.3	18.4	4.8	0	35	3.1	8.4
DYS1−10	4152.52	0.88	37.3	32.5	7	13.4	6.6	3.2	0

compared, and changes in gas flow characteristics in shale samples under simulated mining conditions were discussed.

2. SAMPLES AND METHODS

2.1. Sample Description. The Upper Permian Longtan Formation and the Lower Silurian Longmaxi Formation are two sets of organic-rich shale formations in the Sichuan Basin. The Longtan Formation was formed in a marine−continental transitional sedimentary environment, with lithology consisting of shale, coal, limestone, and sandstone. In the southeastern part of the Sichuan Basin, the Longtan Formation is widely distributed and relatively stable, with a thickness ranging from 70 to 80 m. The organic-rich shale in this area of the Longtan Formation has a thickness of about 40m, with a mean total organic carbon content of 3.23%, and the maturity stage in the overmature stage, with a Ro range of 1.96−2.40%.[43] The Wufeng−Longmaxi Formation is the only shale formation system that has achieved commercial development of shale gas in China. The shale formation has a thickness of approximately 90 m, formed in a depositional environment of shallow−deep water shelf facies. The high-quality shale gas reservoirs are siliceous shale and carbonaceous shale in lithology, with a mean total organic carbon content of 3.50% and the maturity stage in the overmature stage.[46] In this study, two shale core samples from the Longmaxi Formation and Longtan Formation of the DYS1 well in the southeastern part of the Sichuan Basin were used, as shown in Figure 1, with sample numbers DYS1−4 and DYS1−10, at depths of approximately 2991 and 4152 m. Subsequently, the core samples were processed into standard core columns with a diameter of 2.5 cm, with sample numbers DYS1−4P (transitional shale parallel to bedding), DYS1−4C (transitional shale perpendicular to bedding), DYS1−10P (marine shale parallel to bedding), and DYS1−10C (marine shale perpendicular to bedding). The mineral composition of the shale samples is shown in Table 1. The minerals in the deep marine shale are dominated by quartz and clay minerals, with contents of 37.3 and 32.5%, and the minerals in the marine−continental transitional shale are dominated by quartz and dolomite, with contents of 30.3 and 35%, respectively. The contents of feldspar and dolomite in the marine shale are 7 and 13.4%, respectively, higher than that in the marine−continental transitional shale. Figure 2 depicts the morphology of the pore size distribution in the samples. Both the deep marine shale and the marine−continental transitional shale are mainly composed of mesopores (2−50 nm), with developed micropores (<2 nm) in the deep marine shale and numerous macropores (>50 nm) in the marine−continental transitional shale. According to the nitrogen adsorption results, the average pore sizes of the deep marine shale and the marine−continental transitional shale are 5.79 and 9.38 nm, respectively.[47] For a detailed analysis of the mineral, organic matter, and pore characteristics of the experimental samples, please refer to the literature.[47]

2.2. Experimental Setup and Method. In this study, the PoroPDP-200 full-automatic overburden porosity and permeability measurement instrument produced by the American Core Company was used to measure the porosity and

https://doi.org/10.1021/acsomega.3c10441
ACS Omega 2024, 9, 22016−22030

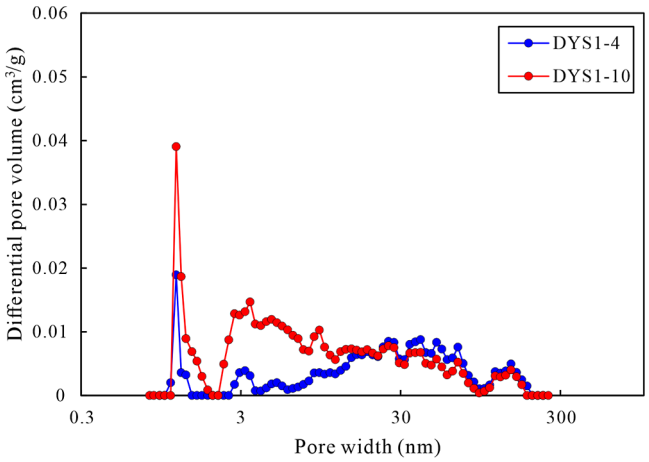

Figure 2. Pore size distributions for experimental samples.

permeability of the samples under overburden pressure. During the test process, the porosity was measured using helium gas at a pressure of 200 psi, which was calculated by Boyle's law. In this study, the apparent permeability under different C_p and P_p conditions was measured using the pressure pulse decay technique, with nonadsorptive gas N_2 as the testing gas.[14,31] Although the steady-state method has been widely used for apparent permeability testing, the pressure pulse decay method has significant advantages in measuring the permeability of low-permeability media. The pressure pulse decay method calculates the permeability by measuring the pressure change, while the steady-state method calculates the permeability by measuring the gas flow rate, making it easier to detect the small pressure changes in low-permeability media compared to the extremely small flow rates.[32,48] To avoid the influence of temperature changes on the test results, the entire system, except for the gas cylinder and computer, was placed in a 22 °C thermotank (Figure 3). The testing process is as follows: (1) The sample is

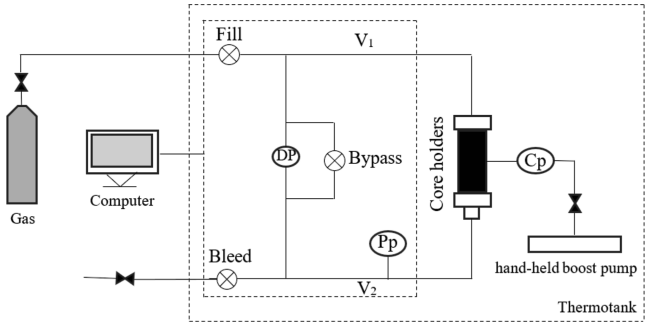

Figure 3. Schematic diagram of the experimental apparatus setup.

placed in a drying oven at 50 °C for more than 12 h before the test to remove moisture and residual hydrocarbon substances from the core and then placed in a 22 °C desiccator for 5 h before the permeability test. (2) Before sample testing, a system leak test was conducted to ensure no leakage. After confirming the integrity of the system, the sample was placed in the core holder, and the confining pressure was increased to the target test value using a hand-held pressure pump. The valve of the pressure pump was then closed. (3) The "Fill" valve is opened to increase the gas pressure (pore pressure) to the target test value. After the pressure stabilizes, the testing begins. The "Fill" valve is automatically closed to allow gas injection into the core, ensuring that the gas pressure in the core is consistent with the pressure in the entire system. Subsequently, a differential pressure (DP) of 0−0.34 MPa (<5psi) is established between the upstream and downstream. (4) When the differential pressure is established, the "Bypass" valve is closed, and the downstream gas chamber pressure and the pressure of the differential pressure sensor DP are automatically detected. The upstream pressure is obtained based on the downstream pressure plus the DP value. During this process, the value of the DP decays linearly with time. When DP decays to 0, the system pressure is the average pressure, and the instrument will automatically stop the test. Finally, the "Bleed" valve is opened to release the gas pressure. After the gas pressure is released, the pressure pump valve is opened, the confining pressure is released, and the core sample is taken out to complete the test. The system will automatically calculate the value of the apparent permeability.

The apparent permeability is calculated by the following equation[49]

$$K = \alpha\mu c_g \frac{L}{S}\left(\frac{1}{1/V_{up} + 1/V_{down}}\right),\ \alpha = -\frac{\ln(DP)}{\Delta t} \quad (1)$$

where α is the gas attenuation index, μ is the kinetic viscosity of nitrogen, obtained through the database of the National Institute of Standards and Technology (NIST), L and S are the length and cross-sectional area of the core, respectively, and c_g is the gas compression coefficient, which is calculated by the following equation[49]

$$c_g = \frac{1}{p} - \frac{1}{z}\frac{dz}{dp} \quad (2)$$

where p represents the average gas pressure and z is the gas compressibility factor. According to the NIST N_2, the variation of the z value with pressure is very small and is approximated to be 1 in this paper.

In laboratory conditions, there is often a so-called "hysteresis effect" in the measurement of overburden permeability; that is, the permeability under the current stress state is influenced by the previous test stress. To restore the experimental conditions to the original reservoir state and ensure that the test data more accurately reflects the deformation characteristics of the underground reservoir rocks, prestressing treatment is usually required before permeability measurement.[50] In this study, each core sample was prestressed by placing the sample in the core holder, maintaining a confining pressure of 50 MPa, pore pressure at 10 MPa for 12 h, and then sequentially reducing the pore pressure to determine the permeability value. The confining pressure was reduced, and the above processing steps and measurements were repeated.[51] As shown in Figure 4, there is a significant difference in the permeability values between samples before and after prestressing treatment; there is a significant difference between the permeability values of the samples in the loading and unloading process before the prestressing treatment under overburden pressure, while there is almost no difference between the permeability values of the samples after the prestressing treatment in the loading and unloading process.

In this study, to characterize the molecular slippage effect of porous media, different confining pressures and pore pressures were maintained during the testing process, and a series of permeability values were measured. The confining pressure (C_p) was fixed at 50 MPa, and the pore pressure (P_p) was initially set

https://doi.org/10.1021/acsomega.3c10441
ACS Omega 2024, 9, 22016−22030

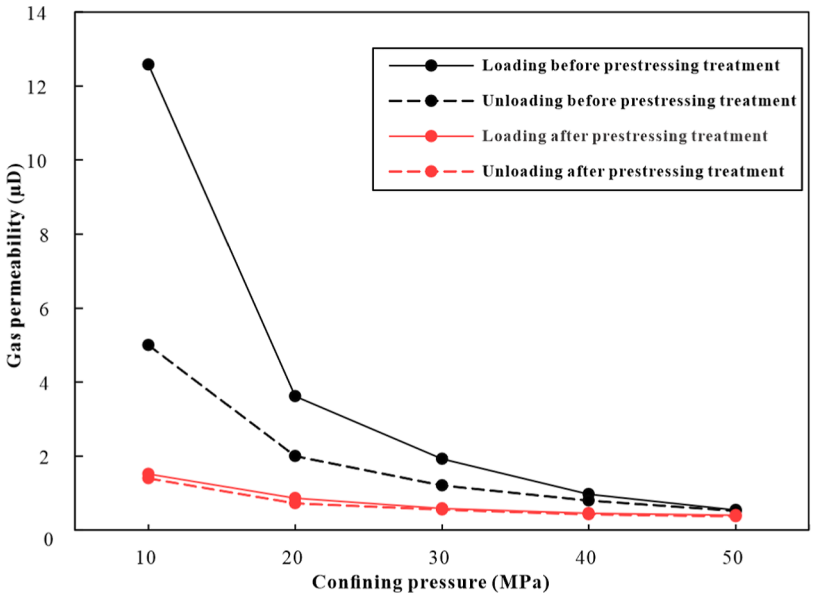

Figure 4. Prestressing treatment of sample DYS1−10P.

at 10 MPa, with permeability measurements taken for every 2 MPa decrease in P_p until it reached the minimum pressure of 2 MPa. Subsequently, C_p was decreased incrementally to 10 MPa, and P_p was measured at intervals of 2 MPa, until the end of the testing, resulting in a total of 23 permeability tests for each sample. Throughout the testing process, C_p was always greater than P_p.

3. RESULTS AND DISCUSSION

In this experiment, porosity ranges from 6.16 to 6.50% for deep marine samples and 2.12−2.34% for marine−continental transitional samples; parallel bedding direction permeability ranges from 0.32 to 1.70 μD for deep marine samples and 0.61−2.60 μD for transitional samples; perpendicular bedding direction permeability ranges from 0.8 to 9.8 nD for deep marine samples and 1.6−6.4 nD for transitional samples (Figure 5). The porosity of the deep marine shale is greater than that of the marine−continental transitional shale. The permeability in the perpendicular direction of the deep marine shale is greater than that of the transitional shale, while the permeability in the parallel direction is similar. There is a positive correlation between the porosity and permeability of shale samples in this study. The shale pore system and mineral composition may affect the anisotropy of shale permeability. With increasing the confining pressure, the permeability of shale gradually decreases. As the pore pressure increases from 2 to 10 MPa, the shale permeability shows a trend of first decreasing and then increasing. The permeability value is higher when the pore pressure is relatively low, which may be attributed to the influence of the molecular slippage effect.

Theoretically, deep marine shale formations have a greater degree of compaction compared to transitional shale formations, resulting in lower nanoscale porosity. However, the tested deep marine shale exhibits higher porosity and permeability compared to the transitional shale. The Ordovician-Silurian formations in the Sichuan Basin have undergone deep burial (depths exceeding 6000 m) and subsequent uplift, with the current depth primarily controlled by uplift intensity.[52] Wang et al. suggested that the porosity of shale is jointly controlled by lithology, burial depth, and fluid pressure.[53] In the deep shale gas reservoirs of the Sichuan Basin, high fluid pressure provides excellent preservation conditions for shale porosity, resulting in higher porosity. Compared to the transitional shale, deep marine shale exhibits lower TOC content and higher quartz content, indicating that the porosity of deep marine shale is primarily associated with quartz, consistent with previous studies.[47] Quartz can act as a rigid framework to inhibit the compaction of deep shale,[54] providing favorable conditions for gas transport in nanopores.

3.1. Klinkenberg Correction to Calculate the Intrinsic Permeability. To better investigate the characteristics of permeability, this study used response surface models to fit the permeability data.[55] Response surface methodology, an empirical modeling approach that does not require any assumptions, was used to fit the experimental data and obtain an empirical model. The model aims to find the most suitable empirical quadratic surface for the permeability measurement value, which is controlled by the confining pressure (C_p) and the pore pressure (P_p). The preliminary transformation of the independent variable data is carried out to reduce the fitted variance and improve the fitting accuracy.[56−58] The method steps are as follows. (1) Perform a Box−Cox transformation on the measured raw data, with the transformation form as

$$K^{(\lambda)} = (K_g{}^{\lambda} - 1)/\lambda \tag{3}$$

The transformed data $K^{(\lambda)}$ is obtained, where λ is the transformation coefficient ranging from −3 to 3. When $\lambda = 0$, it represents a logarithmic transformation. Box suggested using the maximum likelihood method to determine the most suitable transformation coefficient λ.[59] (2) Fit the transformed data $K^{(\lambda)}$ into a quadratic response surface model, represented as

$$K^{(\lambda)} = a_1 + a_2C_p + a_3P_p + a_4C_p{}^2 + a_5C_pP_p + a_6P_p{}^2 \tag{4}$$

Among them, $a_1 \sim a_6$ are the fitting coefficients calculated through the least-squares method and are dimensionless.

(3) Conduct an F-test and perform a significance test on the fitting coefficients. The F-test is used to determine whether the regression model is significant and to evaluate the goodness of fit. The F-value is the ratio of the regression mean square to the

https://doi.org/10.1021/acsomega.3c10441
ACS Omega 2024, 9, 22016−22030

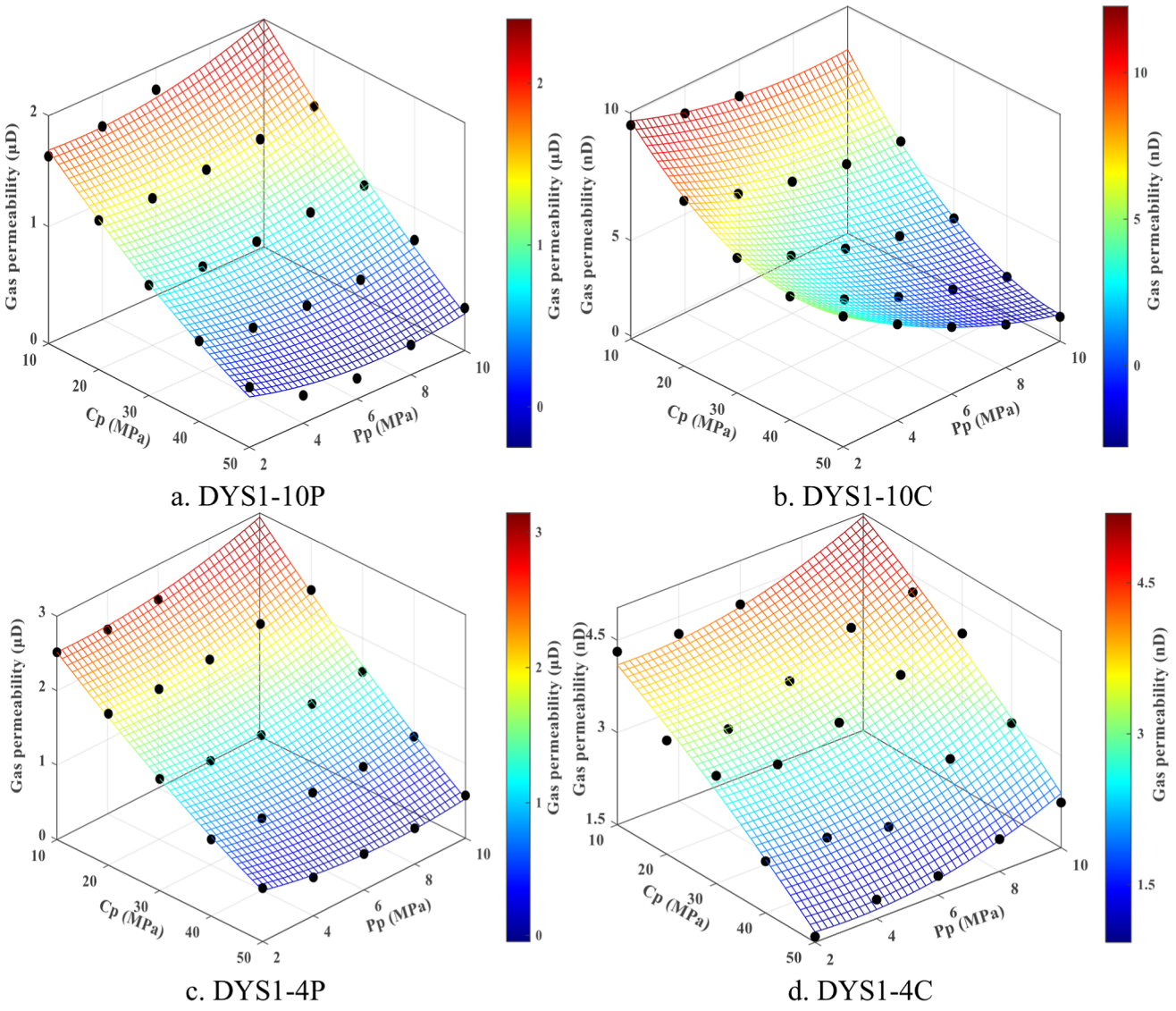

Figure 5. Three-dimensional surfaces of kg for the samples obtained with the response surface model (a. DYS1−10P, b. DYS1−10C, c. DYS1−4P, and d. DYS1−4C).

error mean square. Box considered that the F value is greater than or equal to 10 times the percentile of the F distribution to ensure the effectiveness of fitting the experimental data, and generally, the percentile of the F distribution is taken as 95%.[60]

(4) Calculate the nonlinear effective stress coefficient n based on the fitted model, while satisfying the F-test criterion.

$$n(C_p, P_p) = -\frac{(\partial K/\partial P_p)}{(\partial K/\partial C_p)} = -\frac{(\partial K^{(\lambda)}/\partial P_p)}{(\partial K^{(\lambda)}/\partial C_p)} = -\frac{a_3 + a_5 C_p + 2a_6 P_p}{a_2 + 2a_4 C_p + a_5 P_p} \quad (5)$$

The nonlinear effective stress coefficient n can be calculated for different C_p and P_p once a_i is determined.

(5) Finally, the apparent permeability data K_t obtained through this model is

$$K_t = (\lambda K^{(\lambda)} + 1)^{1/\lambda} \quad (6)$$

And the effective stress is $P_e = C_p - nP_p$. To explore the relationship between the permeability and effective stress, by providing parameters P_e and P_p, the values of C_p and n can be calculated to obtain the corresponding apparent permeability values.

The intrinsic permeability is obtained by the Klinkenberg correction of the apparent permeability. In 1941, Klinkenberg proposed that under the same effective stress, the apparent permeability value of the sample is linearly related to the reciprocal of the pore pressure, and the intercept on the ordinate axis represents the intrinsic permeability, the formula is[22]

$$K_g = K_\infty \left(1 + \frac{b}{P_p}\right) \quad (7)$$

where K_g represents the apparent permeability, K_∞ represents the intrinsic permeability, and b is the Klinkenberg factor, which is related to the pore geometry and size. The larger the value of b,

https://doi.org/10.1021/acsomega.3c10441
ACS Omega 2024, 9, 22016−22030

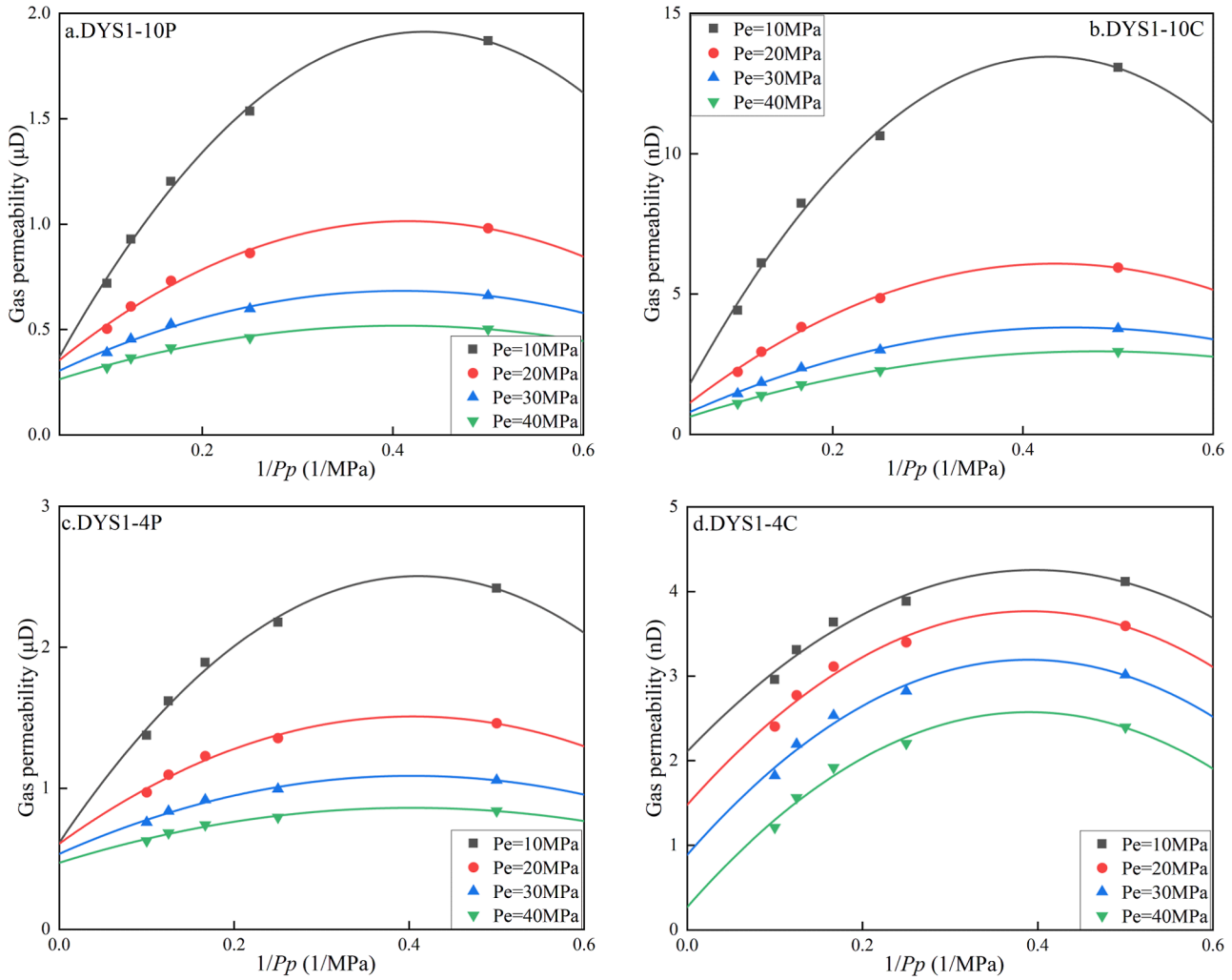

Figure 6. Klinkenberg plots of samples (a. DYS1−10P, b. DYS1−10C, c. DYS1−4P, and d. DYS1−4C).

the greater the contribution of the slippage effect to the apparent permeability.[22]

However, in recent years, it has been observed by some scholars that the Klinkenberg linear model cannot fit the apparent permeability data well in low-permeability media.[24,61] In 2014, a quadratic extension model for low-permeability porous media was proposed by Ashrafi and other scholars, building upon the Klinkenberg linear model.[26] The formula is given as

$$K_g = K_\infty \left(1 + \frac{b}{P_p} - \frac{d}{P_p^2}\right) \quad (8)$$

In the formula, d is a parameter related to the pore size. In high-permeability media, the value of d tends to be 0, the same as the linear model. The expanded model shows that the apparent permeability (K_g) has a quadratic relationship with the inverse of gas pressure ($1/P_p$). Only in low-permeability media with small flow apertures, the value of d will increase, causing the straight line to bend, which leads to the deviation of the linear Klinkenberg model fitting.

In this study, a quadratic extension model was used to fit the apparent permeability data, and the results of the Klinkenberg correction are shown in Figure 6. The corresponding intrinsic permeability K_∞, b, and d can be obtained based on the fitted relationship (Table 2).

The intrinsic permeability in the parallel bedding direction of the deep marine shale is 0.18−0.26 μD, while in the

Table 2. Results and Parameters of the Klinkenberg Correction

sample	effective stress (MPa)	K_∞	b	d
DYS1−10P	10	0.26 μD	32.00	10.48
DYS1−10P	20	0.22 μD	25.20	4.93
DYS1−10P	30	0.19 μD	12.37	2.92
DYS1−10P	40	0.18 μD	8.50	1.98
DYS1−10C	10	1.81 nD	38.36	79.72
DYS1−10C	20	1.23 nD	47.35	29.98
DYS1−10C	30	0.82 nD	51.34	17.40
DYS1−10C	40	0.63 nD	68.00	11.82
DYS1−4P	10	0.62 μD	14.97	11.21
DYS1−4P	20	0.61 μD	7.34	5.52
DYS1−4P	30	0.54 μD	5.12	3.41
DYS1−4P	40	0.47 μD	4.08	2.39
DYS1−4C	10	2.11 nD	5.13	13.65
DYS1−4C	20	1.48 nD	7.93	15.02
DYS1−4C	30	0.89 nD	13.30	15.18
DYS1−4C	40	0.27 nD	43.71	15.16

https://doi.org/10.1021/acsomega.3c10441
ACS Omega 2024, 9, 22016−22030

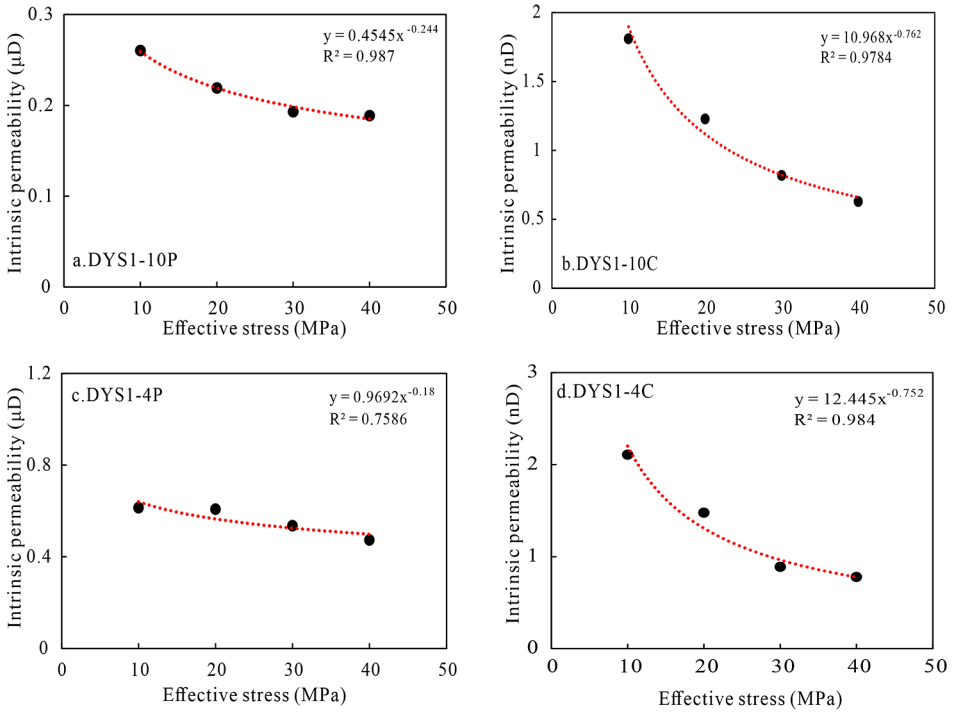

Figure 7. Intrinsic permeability stress sensitivity of samples (a. DYS1−10P, b. DYS1−10C, c. DYS1−4P, and d. DYS1−4C).

perpendicular bedding direction, it is 0.63−1.81 nD. The intrinsic permeability of the marine−continental transitional shale is 0.47−0.62 μD in the parallel bedding direction and 0.27−2.11 nD in the perpendicular bedding direction. The intrinsic permeability of the marine−continental transitional shale is slightly higher than that of the deep marine shale, and the permeability in the parallel bedding direction of shale is still 1 order of magnitude higher than that in the perpendicular bedding direction.

The Klinkenberg factor b reflects the relative contribution of the slippage effect to the apparent permeability. This study found that the Klinkenberg factor b of the deep marine shale is greater than that of the marine−continental transitional shale, and the b value in the perpendicular bedding direction of shale samples is greater than that in the parallel bedding direction. This preliminary indicates that the relative contribution of the slippage effect to the apparent permeability is greater in the deep marine shale than in the marine−continental transitional shale, with the perpendicular bedding direction of shale samples being greater than the parallel bedding direction.

Previous studies have shown a negative correlation between d and the square of the aperture size. This study found that the d value of the deep marine shale in the perpendicular bedding samples ranges from 11.82 to 79.72, and the d value of the marine−continental transitional shale ranges from 13.65 to 15.16. The deep marine shale has a larger d value than the marine−continental transitional shale. The average apertures obtained from nitrogen adsorption are 5.79 and 9.38 nm for the two types of shale, respectively. The deep marine shale has a smaller average aperture. The smaller the aperture, the larger the d value, which is consistent with previous findings.[26]

3.2. Intrinsic Permeability and Stress Sensitivity. The evolution relationship between the intrinsic permeability and the effective stress is shown in Figure 6. The greater the effective stress, the smaller the intrinsic permeability, indicating that the effective stress may cause the shrinkage of the flow channel during the experimental process. In this study, the intrinsic permeability value decreases exponentially with the increase of the effective stress, as represented by[11]

$$K_\infty = K_0 P_e^{-\gamma} \tag{9}$$

In the equation, K_0 represents the intrinsic permeability when the effective stress equals 0, γ is the compressibility index of permeability, and a higher γ value signifies a larger variation in permeability with the effective stress, indicating a higher stress sensitivity of permeability. The γ values, as shown in Figure 7, decrease in the following order: DYS1−10C > DYS1−4C > DYS1−10P > DYS1−4P, indicating a stronger stress sensitivity in the deep marine shale compared to the marine−continental transitional shale. The stress sensitivity of the intrinsic permeability in the perpendicular bedding direction of shale is greater than that in the parallel bedding direction. The clay mineral content in the deep marine shale is higher than that in the marine−continental transitional shale, as indicated in Table 1. This stress sensitivity is largely controlled by the clay mineral content in the samples, which is consistent with the findings of other researchers.[21] Chen believes that in addition to the influence of bedding surfaces, large and small pores are mainly distributed along the bedding surfaces, and clay minerals are often distributed parallel to the bedding surfaces,[62] resulting in more clay mineral pores in the perpendicular bedding direction. Under prolonged compaction, the rock framework in the parallel bedding direction of shale is difficult to change under stress, while the easily compressible clay mineral pores in the perpendicular bedding direction are more prone to deformation under stress.

3.3. Relative Contribution of the Molecular Slippage Effect. Currently, it is believed that the deviation of apparent permeability from intrinsic permeability is caused by the molecular slippage effect. The specific manifestation of the molecular slippage effect is that, under the same effective stress, the apparent permeability increases with the decrease in pore

https://doi.org/10.1021/acsomega.3c10441
ACS Omega 2024, 9, 22016−22030

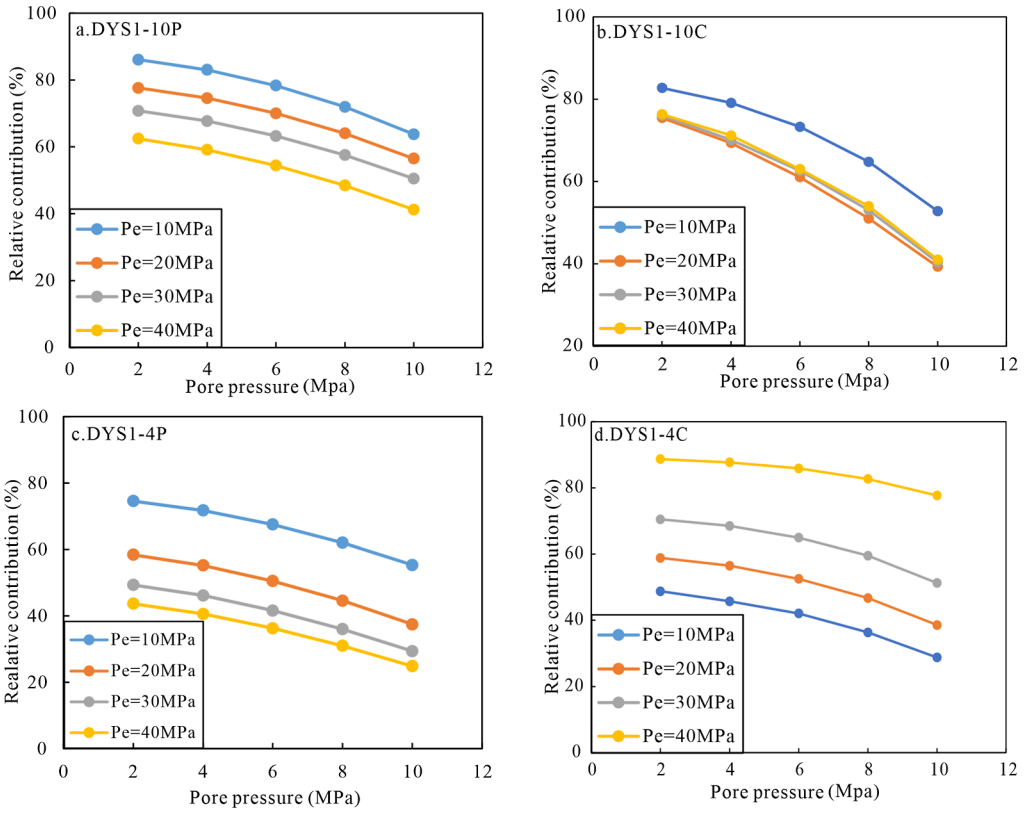

Figure 8. Relative contribution of the molecular slippage effect on the apparent permeability of samples (a. DYS1−10P, b. DYS1−10C, c. DYS1−4P, and d. DYS1−4C).

pressure.[63] According to the Klinkenberg expanded equation, the apparent permeability maintains a quadratic relationship with the inverse of the pore pressure. The relative contribution of the molecular slippage effect to the apparent permeability, denoted as C, is calculated in this study.

$$C = \frac{K - K_\infty}{K} \times 100\% \tag{10}$$

Figure 8 represents the relative contribution of the molecular slippage effect on the apparent permeability of experimental samples under different stress conditions. The contribution of the molecular slippage effect to the apparent permeability under experimental conditions depends on pore pressure and effective stress. The relative contribution of the molecular slippage effect to the apparent permeability of the sample gradually diminishes as the pore pressure increases from 2 to 10 MPa. The relative contribution of the slippage effect to permeability in deep marine shale samples is greater than that in the marine−continental transitional shale samples, and the relative contribution in the perpendicular bedding direction is larger than that in the parallel bedding direction. With the increase in the effective stress, the relative contribution in the parallel bedding direction of shale decreases, while the contribution in the perpendicular bedding direction increases.

The relative contribution also represents the amount by which the apparent permeability deviates from the intrinsic permeability of the sample. Under the same effective stress conditions, the apparent permeability of the deep marine shale deviates further from the intrinsic permeability, reflecting a stronger stress sensitivity of the deep marine shale. With the increase in the effective stress, both the apparent permeability and the intrinsic permeability of shale decrease. The perpendicular bedding direction of the sample exhibits strong stress sensitivity, with a larger decrease in intrinsic permeability and an increased relative contribution. The intrinsic permeability in the parallel bedding direction of the sample decreases to a lesser extent, resulting in a decreased relative contribution. The characteristics of the evolution of the slippage effect with effective stress will be further discussed.

3.4. Gas Transport Mechanism in the Nanoscale Pores.

Shale gas primarily exists in four modes of occurrence: free gas in fractures, free gas in pores, gas adsorbed on pore walls, and gas dissolved in kerogen.[64] Depending on its modes of occurrence, shale gas exhibits various transport mechanisms. Shale with macropores, mesopores, and micropores exhibits different dominant transport mechanisms and corresponding diffusion abilities.[65] In shale with macropores, the pore diameter is significantly greater than the mean free path of gas molecules, and the collision frequency between gas molecules is much higher than the collision frequency between gas molecules and pore walls, leading to predominant continuous gas flow.[66] Decreasing pore size or gas pressure in shale increases the mean free path of gas molecules. If the pore size is similar to the mean free path of gas molecules, the collision between gas molecules and pore walls becomes significant, leading to slip flow, transition flow, or Knudsen diffusion. The transport capacity decreases as the pore size decreases.[66,67] Surface diffusion occurs on the pore walls when gas molecules are adsorbed.[68,69] When the gas phase pressure increases or the pore size decreases further, the adsorbed gas molecules form multiple layers, resulting in multilayer adsorption diffusion.[70] When the pore size of shale is extremely small and comparable to the diameter of gas molecules, only single-molecule transport is possible, and the moving gas molecules continuously collide with the pore

https://doi.org/10.1021/acsomega.3c10441
ACS Omega 2024, 9, 22016−22030

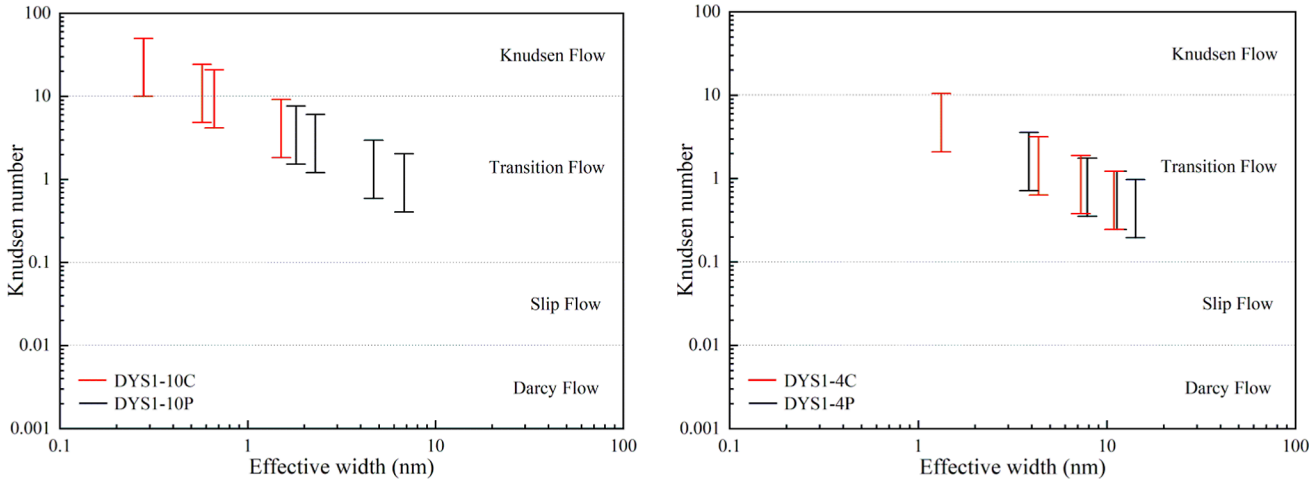

Figure 9. Knudsen number and gas flow mechanisms of samples.

walls, leading to configurational diffusion.[66,71] The classification methods for the new nanopore phase gas transport mechanisms proposed by most scholars still rely on the Knudsen number criterion.[40] The coexistence of multiscale pore structures and various transport flow regimes makes gas transport in shale highly complex.[72,73] Researchers have developed a series of gas transport models considering multiple mechanisms based on the background of shale reservoirs. However, these models have certain limitations due to various factors affecting gas transport in nanopores, including the slippage effect, stress effect, adsorption, desorption, surface diffusion, and real gas effect.[74−77] In this study, we only analyzed the seepage mechanism in nanopores considering the stress effect and slippage effect through conventional experimental methods with low adsorption gas N_2.

The stress effect and the gas slippage effect are competitive, meaning that an increase in the effective stress leads to a decrease in the apparent permeability, while the gas slippage effect increases the apparent permeability. In low-permeability porous media, due to the presence of the molecular slippage effect, gas permeability often deviates from Darcy's law, leading to changes in the gas transport behavior. The shale gas flow mechanisms are complex and diverse, and conventional methods are unable to accurately and comprehensively describe the flow process. According to current research, gas transport is determined by the combination of different flow mechanisms in different pore sizes.[78,79] It is currently believed that gas transport behavior in porous media is composed of two flow regimes: Darcy flow and Knudsen flow. The flow regime division is usually defined by the Knudsen number (Kn), expressed as

$$Kn = \frac{\lambda}{D} \tag{11}$$

In the equation, λ represents the mean free path of gas molecules, which is related to the gas pressure (P_p), the kinetic diameter of gas molecules (δ), and the temperature (T). D represents the flow channel diameter. Typically, λ is defined as

$$\lambda = \frac{K_B T}{\sqrt{2}\,\pi\delta^2 P_p} \tag{12}$$

In the equation, K_B is the Boltzmann constant, equal to 1.3806×10^{-23} J/K; for nitrogen, δ is 0.364 nm; during the experimental process, the temperature is constant, so the mean free path of the molecules is only related to the gas pressure. λ is inversely proportional to P_p, meaning that the larger the P_p, the smaller the λ.

The Knudsen number is a dimensionless parameter that defines the ratio of the mean free path of gas molecules to the flow channel aperture, reflecting the relative collision frequency between gas molecules and between gas molecules and the pore walls. A small Knudsen number ($Kn < 0.01$) indicates that the mean free path of gas molecules is much smaller than the flow channel aperture, i.e., collisions between gas molecules are more frequent than between gas molecules and the pore wall. In this case, the gas is assumed to behave as a viscous fluid, known as the Darcy flow. Conversely, a large Knudsen number ($Kn > 10$) represents another flow regime, known as Knudsen flow, where collisions between gas molecules and the pore wall are more frequent, and collisions between gas molecules can be neglected, with the gas flow behavior mainly characterized by the back and forth collisions of individual molecules with the pore wall. The transition flow between these two regimes is further divided into two forms: slip flow and transition flow.[63]

Currently, the Knudsen number is commonly used to characterize the strength of the slippage effect, and when $K_n > 0.01$, it represents a significant slippage effect. In nanoporous media, the gas transport mechanism is no longer governed by Darcy's law due to the influence of the slippage effect. Depending on the magnitude of the Knudsen number, the gas transport mechanism in nanopores, i.e., gas flow regimes, is divided into Darcy flow ($Kn < 0.01$), slip flow ($0.01 < Kn < 0.1$), transition flow ($0.1 < Kn < 10$), and Knudsen flow ($Kn > 10$).

According to the formula, the effective aperture (D, nm) of the fissure flow channel can be calculated with the Klinkenberg parameter b.[80]

$$D = \frac{16c\mu}{b}\left(\frac{2RT}{\pi M}\right)^{1/2} \tag{13}$$

where parameter c is the Adzumi constant currently believed to be equal to 0.9, μ is the gas dynamic viscosity, R is the gas constant, and M is the molar mass of the gas molecule. This formula applies to the narrow-type flow channel and is widely used in shale.

To characterize the gas flow behavior of the samples, the Knudsen number and effective flow width were calculated in this study, and their flow mechanisms were classified (Figure 9). The

https://doi.org/10.1021/acsomega.3c10441
ACS Omega 2024, 9, 22016−22030

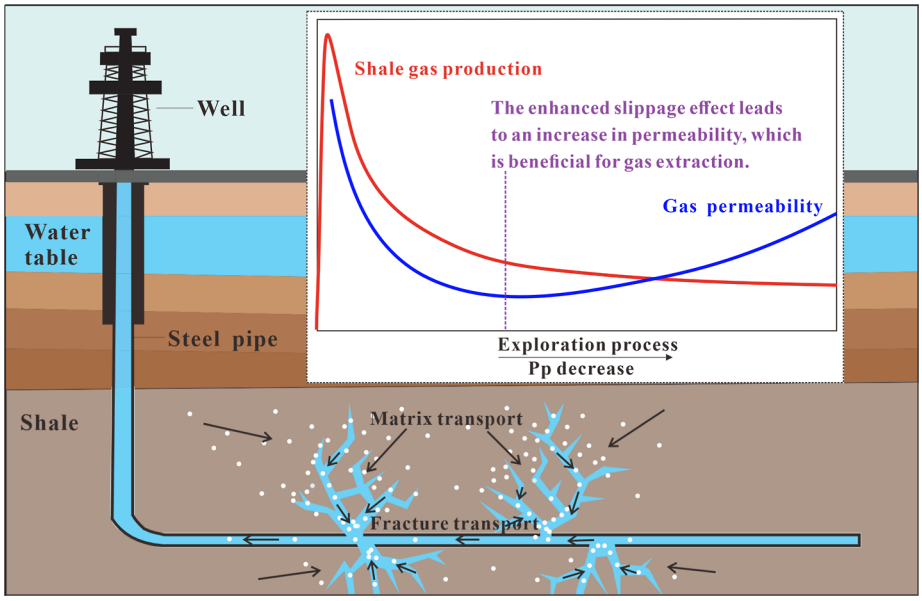

Figure 10. Gas transport during shale gas development.

flow mechanisms in the deep marine shale are transition flow and Knudsen flow, while that of the marine−continental transitional shale is transition flow. On a macroscopic level, the porosity and gas permeability of the deep marine shale are greater than those of the marine−continental transitional shale, providing favorable conditions for gas transport in the nanoscale pores of the deep marine shale. On a microscopic level, compared to the marine−continental transitional shale, the deep marine shale has a smaller average pore size and a greater number of micropores as determined by nitrogen adsorption tests.[47] These micropores are closer in size to the diameter of N_2 molecules (0.364 nm). Gas molecules in the nanopores collide more frequently with the pore walls than with each other, either through more frequent collisions or by repeatedly colliding with the pore walls in a single-molecule form. Additionally, the study found that the calculated effective flow aperture is smaller than the measured average pore size, and the difference between the two may be attributed to other influencing factors such as gas adsorption and diffusion.[40] Moreover, the difference in the deep marine shale is larger, indicating a greater contribution to the gas transport mechanism.

This indicates that the slippage effect in the deep marine shale is stronger than in the marine−continental transitional shale, possibly due to the development of more micropores and smaller pore sizes in the deep marine shale. The slippage effect in the perpendicular bedding direction of the shale samples is stronger than that in the parallel bedding direction, which is attributed to the smaller effective flow width in the vertical bedding direction compared to the parallel bedding direction. With the increase in the effective stress, the capillary aperture in the perpendicular bedding direction of the shale samples decreases, the flow channel reduces, and the effective flow width decreases relatively, causing the slippage effect to strengthen. The capillary aperture in the parallel bedding direction of the shale samples decreases to a smaller extent due to lower stress sensitivity, and the closure of clay micropores in the parallel bedding direction leads to a relatively larger proportion of larger pores, resulting in a relative increase in the effective flow width and a weakening of the slippage effect.

3.5. Geological Significance. Shale gas reservoirs are unconventional oil and gas resources, with permeability generally in the nanodarcy range. These complex and heterogeneous gas reservoirs require innovative exploration and completion strategies to economically produce natural gas. Despite the widespread estimates of significant natural gas reserves in shale gas reservoirs, achieving economically viable flow rates technically remains challenging, partly due to an insufficient understanding of the fluid transport processes in the matrix and fracture systems of these rock types. However, shale formations still possess the conditions for shale gas occurrence, and shale gas production enhancement and stabilization can be achieved through reservoir modification and other production measures.[81]

Extensive research and practice have shown that the accuracy of shale stress sensitivity assessment directly affects the accuracy of calculating in situ reserves of shale oil and gas. The effective determination of the conversion standard from conventional reservoir physical parameters to in situ physical parameters and, consequently, the calculation of true reserves, can only be achieved through a clear understanding of the stress sensitivity law of reservoirs. Stress sensitivity serves as a crucial parameter in determining the appropriate pressure drop for production in oilfield operations. Only by quantitatively clarifying the stress sensitivity characteristics of the reservoir can safe and efficient production of shale oil be achieved; that is, the accuracy of stress sensitivity understanding directly affects the degree of improvement in the recovery rate.[82]

In the process of shale gas development, the gas transport process can be divided into two stages: In the first stage, known as the matrix transport stage, gas from the pores inside the source rocks enters the fracture network system through matrix nanochannels. In the second stage, known as the fracture transport stage, gas in the fracture network system enters the wellbore in the form of Darcy flow. The second stage has a fast flow rate and large flow volume, which determines the initial production after the hydraulic fracturing of gas wells. The gas transport speed in the first stage is relatively slow, but it lasts for a long time and is a key factor in determining the long-term stable production capacity of gas wells. From the perspective of

https://doi.org/10.1021/acsomega.3c10441
ACS Omega 2024, 9, 22016−22030

commercial shale gas production, fractures are considered the main pathway for gas production. However, some studies indicate that even in the presence of hydraulic fracturing fractures, the long-term gas production constraint in shale gas is still fluid transport in the matrix. Therefore, shale matrix permeability is one of the key parameters for the sustained production of shale gas wells.

Many actual exploitation data of shale gas fields show that the production of shale gas will generally experience a rapid decline, followed by a slow decline, and finally maintain a stable state.[83,84] For shale gas development, as the continuous reduction of gas inside the pores caused by the exploitation and migration of shale gas, the gas pressure will decrease, and the effective stress borne by the rock framework will gradually increase, leading to internal pore compression and reduced flow channels. The matrix permeability of the shale reservoir will decrease, resulting in a decrease in gas flow, a rapid decline in shale gas production, and at this time, the gas slippage effect is weak, and the gas flow state is in the slip flow range. When the gas pressure decreases to a certain stage and the internal pores are very small, the collision between gas molecules and the pore walls is more frequent than the collision between gas molecules, and the gas flow behavior is more characterized by single-molecule and pore wall collisions, influenced strongly by the molecular slippage effect. The matrix permeability of the shale reservoir will increase, the gas flow rate will increase somewhat, and the shale gas production will slowly decline. At this time, the gas slippage effect is strong, and the gas flow regimes transition from slip flow to transition flow or even Knudsen flow (Figure 10). According to the results of this study, when the pore pressure of the deep marine shale decreases to 6 MPa, the permeability will increase, and the gas flow regimes transition from slip flow to transition flow and Knudsen flow; when the pore pressure of the marine−continental transitional shale decreases to 4 MPa, the permeability increases, and the gas flow regimes transition from slip flow to transition flow. The flow regimes' transition related to the gas slippage effect in the shale matrix transfer process may be the key factor for the continuous stable production of shale gas wells.

The factors affecting the decline rate of shale gas production from horizontal wells have been studied by the researchers. It was found that, in the early stages of production, higher matrix permeability is associated with a slower daily gas production decline. In the later stages of production, the higher the matrix permeability, the higher the daily gas production, and the faster the rate of decline.[85] This indicates that throughout the entire shale gas production process, the daily production of deep marine shale gas, which has higher permeability, consistently exceeds that of marine−continental transitional shale gas. The production of shale gas from the deep marine shale Jiaoye XHF well is 6×10^4 m^3/d, while the Jiyue-Ping 1 well in the marine−continental transitional shale yields 3.5×10^4 m^3/d. When the wellhead pressure drops to 3 MPa, the recoverable reserves of the Jiaoye XHF well increase from 1.1×10^8 to 1.28×10^8 m^3, an increase of 0.17×10^8 m^3.[86] Simulation results of the cumulative gas production after 20 years for the Jiping 1H well show that the ultimate recoverable reserves increase from 4760×10^4 to 5660×10^4 m^3, an increase of 900×10^4 m^3.[87−89] In summary, compared to the marine−continental transitional shale, deep marine shale exhibits greater shale gas production, production rates, and production duration.

4. CONCLUSIONS

Permeability, stress sensitivity, and gas flow mechanisms for the deep marine shale from the Longmaxi Formation and the marine−continental transitional shale from the Longtan Formation in the southeastern Sichuan Basin are analyzed and compared in this study. The following conclusions are obtained.

(1) The porosity and gas permeability of the deep marine shale is greater compared to the marine−continental transitional shale. The elevated fluid pressure in the deep marine shale creates favorable conditions for the preservation of nanopores, leading to a higher nanoporosity in the deep marine shale compared to the middle and shallow shale. The presence of a high quartz content hinders the compaction of deep shale while supporting nanopore channels, thereby increasing the permeability of the deep marine shale compared to the transitional shale.

(2) The intrinsic permeability stress sensitivity of the deep marine shale samples is higher than that of the marine−continental transitional shale, possibly due to differences in mineral content. Additionally, the stress sensitivity of the intrinsic permeability in the perpendicular bedding direction of shale samples is greater than that in the parallel bedding direction, which may be related to the compaction effect of shale bedding.

(3) The flow mechanism of the deep marine shale is transition flow and Knudsen flow, while that of the marine−continental transitional shale is transition flow. The deep marine shale possesses smaller nanopore sizes and a higher quantity of micropores, which create advantageous conditions for gas transport within nanopores. The slippage effect is stronger in the perpendicular bedding direction than in the parallel bedding direction for shale. As the effective stress increases, the slippage effect in the perpendicular bedding direction intensifies, while the slippage effect in the parallel bedding direction weakens.

(4) During the shale gas development process, the decrease in gas pore pressure and the increase in effective stress cause a reduction in permeability, leading to a rapid decline in shale gas production. When the gas pressure decreases to the critical value, the enhanced slippage effect compensates for the decrease in permeability, thereby reducing the rate of decline in shale gas. The critical value of the deep marine shale is higher than that of the transitional shale, indicating that the deep marine shale gas reaches a stable production state earlier. The flow capacity of the deep marine shale is stronger, leading to a longer production time for shale gas wells.

AUTHOR INFORMATION

Corresponding Author

Jing Li − *Northwest Institute of Eco-Environment and Resources, Chinese Academy of Sciences, Lanzhou 730000, China; Key Laboratory of Petroleum Resources Exploration and Evaluation, Gansu Province, Lanzhou 730000, China;* orcid.org/0000-0002-4180-2400; Email: Lj1926@lab.ac.cn

Authors

Liangliang Liu − *Northwest Institute of Eco-Environment and Resources, Chinese Academy of Sciences, Lanzhou 730000, China; Key Laboratory of Petroleum Resources Exploration and Evaluation, Gansu Province, Lanzhou 730000, China;*

https://doi.org/10.1021/acsomega.3c10441
ACS Omega 2024, 9, 22016−22030

University of Chinese Academy of Sciences, Beijing 100049, China; orcid.org/0000-0002-5431-4959

Shixin Zhou − *Northwest Institute of Eco-Environment and Resources, Chinese Academy of Sciences, Lanzhou 730000, China; Key Laboratory of Petroleum Resources Exploration and Evaluation, Gansu Province, Lanzhou 730000, China;* orcid.org/0009-0004-6745-1508

Gengrong Chen − *Northwest Institute of Eco-Environment and Resources, Chinese Academy of Sciences, Lanzhou 730000, China; Key Laboratory of Petroleum Resources Exploration and Evaluation, Gansu Province, Lanzhou 730000, China; University of Chinese Academy of Sciences, Beijing 100049, China*

Yaoyu Li − *Northwest Institute of Eco-Environment and Resources, Chinese Academy of Sciences, Lanzhou 730000, China; Key Laboratory of Petroleum Resources Exploration and Evaluation, Gansu Province, Lanzhou 730000, China; University of Chinese Academy of Sciences, Beijing 100049, China*

Wenjun Pang − *Northwest Institute of Eco-Environment and Resources, Chinese Academy of Sciences, Lanzhou 730000, China; Key Laboratory of Petroleum Resources Exploration and Evaluation, Gansu Province, Lanzhou 730000, China; University of Chinese Academy of Sciences, Beijing 100049, China*

Hao Wang − *Northwest Institute of Eco-Environment and Resources, Chinese Academy of Sciences, Lanzhou 730000, China; Key Laboratory of Petroleum Resources Exploration and Evaluation, Gansu Province, Lanzhou 730000, China; University of Chinese Academy of Sciences, Beijing 100049, China*

Complete contact information is available at: https://pubs.acs.org/10.1021/acsomega.3c10441

Notes

The authors declare no competing financial interest.

■ ACKNOWLEDGMENTS

This study was funded by the National Nature Science Foundation of China (grant nos. 42172178 and 42372178) and the Project of Stable Support for Youth Team in Basic Research Field, Chinese Academy of Sciences (grant no. YSBR-017).

■ REFERENCES

(1) Zou, C.; Zhao, Q.; Cong, L.; Wang, H.; Shi, Z.; Wu, J.; Pan, S. Development progress, potential and prospect of shale gas in China. *Nat. Gas Ind.* **2021**, *41*, 1−14.

(2) Long, S.; Lu, T.; Li, Q.; Yang, G.; Li, D. Discussion on China's shale gas development ideas and goals during the 14th Five-Year Plan. *Nat. Gas Ind.* **2021**, *41*, 1−10.

(3) Liu, Y.; Liu, D.; Peng, C.; Zhang, R. China's development status of shale gas and progress in key technology research. *Mod. Chem. Ind.* **2022**, *42*, 16−20.

(4) Zou, C.; Yang, Z.; Zhang, G.; Zhu, R.; Tao, S.; Yuan, X.; Hou, L.; Dong, D.; Guo, Q.; Song, Y.; et al. Theory, Technology and Practice of Unconventional Petroleum Geology. *Earth Sci.* **2023**, *48*, 2376−2397.

(5) Jia, C. Z. Breakthrough and significance of unconventional oil and gas to classical petroleum geology theory. *Pet. Explor. Dev.* **2017**, *44*, 1−10.

(6) Zou, C.; Zhao, Q.; Zhang, G.; Xiong, B. Energy revolution: From a fossil energy era to a new energy era. *Nat. Gas Ind.* **2016**, *3*, 1−11.

(7) Dong, D.; Liang, F.; Guan, Q.; Jiang, Y.; Zhou, S.; Yu, R.; Gu, Y.; Zhang, S.; Qi, L.; Liu, Y. Development model and identification evaluation technology of Wufeng-Longmaxi Formation quality shale gas reservoirs in the Sichuan Basin. *Nat. Gas Ind.* **2022**, *42*, 96−111.

(8) Nie, H.; Li, P.; Dang, W.; Ding, J.; Sun, C.; Liu, M.; Wang, J.; Du, W.; Zhang, P.; Li, D.; et al. Enrichment characteristics and exploration directions of deep shale gas of Ordovician- Silurian in the Sichuan Basin and its surrounding areas, China. *Pet. Explor. Dev.* **2022**, *49*, 744−757.

(9) Li, J.; Wang, X.; Hou, L.; Chen, C.; Guo, J.; Yang, C.; Wang, Y.; Li, Z.; Cui, H.; Hao, A.; et al. Geochemical characteristics and resource potential of shale gas in Sichuan Basin. *Nat. Gas Geosci.* **2021**, *6*, 313−327.

(10) Guo, W.; Gao, J.; Li, H.; Kang, L.; Zhang, J.; Liu, G.; Liu, Y. The geological and production characteristics of marine-continental transitional shale gas in China: Taking the example of shale gas from Shanxi Formation in Ordos Basin and Longtan Formation in Sichuan Basin. *Miner. Explor.* **2023**, *14*, 448−458.

(11) Bustin, A. M. M.; Bustin, R. M. Importance of rock properties on the producibility of gas shales. *Int. J. Coal Geol.* **2012**, *103*, 132−147.

(12) Davudov, D.; Moghanloo, R. G. Impact of pore compressibility and connectivity loss on shale permeability. *Int. J. Coal Geol.* **2018**, *187*, 98−113.

(13) Tan, X.; Li, X.; Liu, J.; Zhang, L.; Fan, Z. Study of the effects of stress sensitivity on the permeability and porosity of fractal porous media. *Phys. Lett. A* **2015**, *379*, 2458−2465.

(14) Yang, D.; Wang, W.; Chen, W.; Wang, S.; Wang, X. Experimental investigation on the coupled effect of effective stress and gas slippage on the permeability of shale. *Sci. Rep.* **2017**, *7*, 44696.

(15) Ge, Z.; Li, S.; Zhou, Z.; Lu, Y.; Xia, B.; Tang, J. Modeling and Experiment on Permeability of Coal with Hydraulic Fracturing by Stimulated Reservoir Volume. *Rock. Mech. Rock. Eng.* **2019**, *52*, 2605−2615.

(16) Li, Q.; Xing, H.; Liu, J.; Liu, X. A review on hydraulic fracturing of unconventional reservoir. *Petroleum* **2015**, *1*, 8−15.

(17) Towler, B.; Firouzi, M.; Underschultz, J.; Rifkin, W.; Garnett, A.; Schultz, H.; Esterle, J.; Tyson, S.; Witt, K. An overview of the coal seam gas developments in Queensland. *J. Nat. Gas Sci. Eng.* **2016**, *31*, 249−271.

(18) Heller, R.; Vermylen, J.; Zoback, M. Experimental investigation of matrix permeability of gas shales. *AAPG Bull.* **2014**, *98*, 975−995.

(19) Letham, E. A.; Bustin, R. M. Klinkenberg gas slippage measurements as a means for shale pore structure characterization. *Geofluids* **2016**, *16*, 264−278.

(20) Xiao, W.; Li, T.; Li, M.; Zhao, J.; Zheng, L.; Li, L. Evaluation of the stress sensitivity in tight reservoirs. *Pet. Explor. Dev.* **2016**, *43*, 115−123.

(21) Xiao, W. L.; Jiang, L.; Li, M.; Zhao, J. Z.; Zheng, L. L.; Li, X. F.; Zhang, Z. P. Effect of clay minerals on the effective pressure law in clay-rich sandstones. *J. Nat. Gas Sci. Eng.* **2015**, *27*, 1242−1251.

(22) Klinkenberg, L. J. *The Permeability of Porous Media To Liquids And Gases*; Drilling and Production Practice, 1941.

(23) Chen, C. Multiscale imaging, modeling, and principal component analysis of gas transport in shale reservoirs. *Fuel* **2016**, *182*, 761−770.

(24) Letham, E. A.; Bustin, R. M. The impact of gas slippage on permeability effective stress laws: Implications for predicting permeability of fine-grained lithologies. *Int. J. Coal Geol.* **2016**, *167*, 93−102.

(25) Wu, K.; Chen, Z.; Li, X.; Guo, C.; Wei, M. A model for multiple transport mechanisms through nanopores of shale gas reservoirs with real gas effect-adsorption-mechanic coupling. *Int. J. Heat Mass Transfer* **2016**, *93*, 408−426.

(26) Ashrafi Moghadam, A.; Chalaturnyk, R. Expansion of the Klinkenberg's slippage equation to low permeability porous media. *Int. J. Coal Geol.* **2014**, *123*, 2−9.

(27) Cui, X.; Bustin, A. M. M.; Bustin, R. M. Measurements of gas permeability and diffusivity of tight reservoir rocks: different approaches and their applications. *Geofluids* **2009**, *9*, 208−223.

(28) Li, M.; Bernabé, Y.; Xiao, W. I.; Chen, Z. Y.; Liu, Z. Q. Effective pressure law for permeability of E-bei sandstones. *J. Geophys. Res.: Solid Earth* **2009**, *114*, B07205.

(29) Sun, J.; Yang, Z.; Guo, H.; Xiao, Q.; Hao, M.; Xu, X. Comparative study of tight reservoir permeability using steady-state and unsteady-state methods. *Rock Soil Mech.* **2013**, *34*, 1009−1016.
(30) Xu, X.; Chen, L.; Zhang, Y. Discussion on two issues of test experiment with coal and rock permeability steady state method. *Coal Sci. Technol.* **2016**, *44*, 104−108.
(31) Brace, W.; Walsh, J.; Frangos, W. Permeability Of Granite Under High Pressure. *J. Geophys. Res.* **1968**, *73*, 2225−2236.
(32) de Bilbao, E.; Loison, L.; Hbiriq, Y.; Orgeur, C.; Brassamin, S.; Tonnesen, T.; Poirier, J. Intrinsic permeability of refractories from gas permeability measurements: Comparison of results. *Ceram. Int.* **2018**, *44*, 2900−2910.
(33) Gao, J.; Li, Z. X. Water saturation-driven evolution of helium permeability in Carboniferous shale from Qaidam Basin, China: An experimental study. *Mar. Pet. Geol.* **2018**, *96*, 371−390.
(34) Li, J.; Liu, D.; Yao, Y.; Cai, Y.; Wang, L. Controls of Gas Slippage and Effective Stress on the Gas Permeability of Coal. *Nat. Gas Geosci.* **2013**, *24*, 1074−1078.
(35) Sun, Z.; Zhou, S.; Li, J.; Chen, K.; Zhang, C.; Zhang, Y.; Li, P. Laboratory Research on Gas Transport in Shale Nanopores Considering the Stress Effect and Slippage Effect. *J. Geophys. Res.: Solid Earth.* **2020**, *125*, No. e2019JB018256.
(36) Zhang, R.; Ning, Z.; Yang, F.; Wang, X.; Zhao, H.; Wang, Q. Impacts of nanopore structure and elastic properties on stress-dependent permeability of gas shales. *J. Nat. Gas Sci. Eng.* **2015**, *26*, 1663−1672.
(37) Bowker, K. A. Barnett Shale gas production, Fort Worth Basin: Issues and discussion. *AAPG Bull.* **2007**, *91*, 523−533.
(38) Skoulidas, A. I.; Sholl, D. S.; Johnson, J. K. Adsorption and diffusion of carbon dioxide and nitrogen through single-walled carbon nanotube membranes. *J. Chem. Phys.* **2006**, *124*, 054708.
(39) Wang, H.; Liu, Y.; Dong, D.; Zhao, Q.; Du, D. Scientific issues on effective development of marine shale gas in southern China. *Pet. Explor. Dev.* **2013**, *40*, 615−620.
(40) Wu, K.; Chen, Z. Review of gas transport in nanopores in shale gas reservoirs. *Pet. Sci. Bull.* **2016**, *1*, 91−127.
(41) Wang, H.; Shi, Z.; Zhou, T.; Zhao, Q.; Sun, S.; Qi, L.; Liang, P. Types and characteristics of sweet spots of marine black shale and significance for shale gas exploration: A case study of Wufeng-Longmaxi in southern Sichuan Basin. *Nat. Gas Ind.* **2023**, *43*, 1−13.
(42) Wei, F.; Liu, Z.; Chen, F.; Yuan, T.; Li, F. Characteristics of the deep and ultra-deep shale reservoirs of the Wufeng-Longmaxi formations in the southeastern Sichuan Basin and the significance of shale gas exploration. *Pet. Geol. Exp.* **2023**, *45*, 751−760.
(43) Guo, X.; Hu, D.; Liu, R.; Wei, X.; Wei, F. Geological conditions and exploration potential of Permian marine-continent transitional facies shale gas in the Sichuan Basin. *Nat. Gas Ind.* **2018**, *38*, 11−18.
(44) He, G.; He, X.; Gao, Y.; Zhang, P. Discovery of shale gas of Permian Longtan Formation in Nanchuan area, southeast Sichuan Basin. *Geol. China* **2023**, *50*, 965−966.
(45) Wang, E.; Guo, T.; Liu, B.; Li, M.; Xiong, L.; Dong, X.; Zhang, N.; Wang, T. Lithofacies and pore features of marine-continental transitional shale and gas enrichment conditions of favorable lithofacies:A case study of Permian Longtan Formation in the Lintanchang area, southeast of Sichuan Basin, SW China. *Pet. Explor. Dev.* **2022**, *49*, 1310−1322.
(46) Guo, X.; Li, Y.; Borjigen, T.; Wang, Q.; Yuan, T.; Shen, B.; Ma, Z.; Wei, F. Hydrocarbon generation and storage mechanisms of deep-water shelf shales of Ordovician Wufeng Formation-Silurian Longmaxi Formation in Sichuan Basin, China. *Pet. Explor. Dev.* **2020**, *47*, 204−213.
(47) Li, J.; Liu, L.; Meng, B.; Li, Y.; Zhou, S.; Pang, W. Comparative Study on the Primary Control Factors of Nanopores in Transitional and Deep Marine Shale in the Southeastern Sichuan Basin, China. *Energy Fuels* **2023**, *37*, 7161−7172.
(48) Metwally, Y. M.; Sondergeld, C. H. Measuring low permeabilities of gas-sands and shales using a pressure transmission technique. *Int. J. Rock Mech. Min. Sci.* **2011**, *48*, 1135−1144.
(49) Jones, S. C. A technique for faster pulse-decay permeability measurements in tight rocks. *SPE Form. Eval.* **1997**, *12*, 19−25.
(50) Li, M.; Xiao, W.; Bernabé, Y.; Zhao, J. Nonlinear effective pressure law for permeability. *J. Geophys. Res.: Solid Earth.* **2014**, *119*, 302−318.
(51) Wang, F.; Xiang, Z.; Chen, Z.; Zhang, L. Correct Reservoir Stress Sensitivity Curve By Using Response Surface Method. *J. Southwest Pet. Univ.* **2010**, *32*, 96−99.
(52) Nie, H.; He, Z.; Liu, G.; Du, W.; Wang, R.; Zhang, G. Genetic mechanism of high-quality shale gas reservoirs in the Wufeng-Longmaxi Fms in the Sichuan Basin. *Nat. Gas Ind.* **2020**, *40*, 31−41.
(53) Wang, R.; Nie, H.; Hu, Z.; Liu, G.; Xi, B.; Liu, W. Controlling effect of pressure evolution on shale gas reservoirs:A case study of the Wufeng-Longmaxi Formation in the Sichuan Basin. *Nat. Gas Ind.* **2020**, *40*, 1−11.
(54) Dong, T.; Harris, N. B.; Ayranci, K.; Twemlow, C. E.; Nassichuk, B. R. The impact of composition on pore throat size and permeability in high maturity shales: Middle and Upper Devonian Horn River Group, northeastern British Columbia, Canada. *Mar. Pet. Geol.* **2017**, *81*, 220−236.
(55) Box, G. E. P. *Empirical model-building and response surfaces/George E. P. Box, Norman R. Draper*; Empirical Model-Building and Response Surfaces/George E. P. Box, Norman R. Draper, 1987.
(56) Nair, A.; Makwana, A.; Ahammed, M. The use of response surface methodology for modelling and analysis of water and wastewater treatment processes: a review. *Water Sci. Technol.* **2014**, *69*, 464−478.
(57) Tian, Y.; Zheng, Y.; Zheng, C.; Xiao, H.; Fan, W.; Zou, S.; Wu, B.; Yao, Y.; Zhang, A.; Liu, J. Exploring scale-dependent ecohydrological responses in a large endorheic river basin through integrated surface water-groundwater modeling. *Water Resour. Res.* **2015**, *51*, 4065−4085.
(58) Xing, J.; Wang, S.; Jang, C.; Zhu, Y.; Hao, J. Nonlinear response of ozone to precursor emission changes in China: a modeling study using response surface methodology. *Atmos. Chem. Phys.* **2011**, *11*, 5027−5044.
(59) Box, G. E. P.; Cox, D. R. An Analysis Of Transformations. *J. Roy. Stat. Soc. B* **1964**, *26*, 211−243.
(60) Zheng, L.; Min, L.; Xiao, W.; Zeng, L. Determination of Effective Stress Coefficient of Permeability Using Maximum-Likelihood Function Approach. *Xinjiang Pet. Geol.* **2008**, *29*, 747−749.
(61) Zhang, W.; Wang, Q. Permeability anisotropy and gas slippage of shales from the Sichuan Basin in South China. *Int. J. Coal Geol.* **2018**, *194*, 22−32.
(62) Chen, T.; Feng, X.; Zhang, X.; Cao, W.; Fu, C. Experimental Study On Mechanical And Anisotropic Properties Of Black Shale. *Chin. J. Rock Mech. Eng.* **2014**, *33*, 1772−1779.
(63) Sun, Z.; Zhou, S.; Li, J.; Chen, K.; Zhang, C.; Zhang, Y.; Li, P. Permeability stress sensitivity and gas-slippage effect of low-permeability porous media: An experimental case study of mud-stone/shale of Chang 7 Member of Yanchang Formation in the Ordos Basin. *Geochimica* **2019**, *48*, 624−631.
(64) Swami, V.; Settari, A.; Javadpour, F. A numerical model for multi-mechanism flow in shale gas reservoirs with application to laboratory scale testing. In *SPE Europec Featured at EAGE Conference and Exhibition?*; OnePetro, 2013; SPE: pp SPE-164840-MS.
(65) Post, M. F. Chapter 11 Diffusion in Zeolite Molecular Sieves. In *Studies in Surface Science and Catalysis*; Elsevier, 1991; Vol. *58*, pp 391−443.
(66) Xiao, J.; Wei, J. Diffusion mechanism of hydrocarbons in zeolites-I. Theory. *Chem. Eng. Sci.* **1992**, *47*, 1123−1141.
(67) Wang, M.; Li, Z. Nonideal gas flow and heat transfer in micro-and nanochannels using the direct simulation Monte Carlo method. *Phys. Rev. E: Stat., Nonlinear, Soft Matter Phys.* **2003**, *68*, 046704.
(68) Choi, J.-G.; Do, D.; Do, H. Surface diffusion of adsorbed molecules in porous media: Monolayer, multilayer, and capillary condensation regimes. *Ind. Eng. Chem. Res.* **2001**, *40*, 4005−4031.
(69) Okazaki, M.; Tamon, H.; Toei, R. Interpretation of surface flow phenomenon of adsorbed gases by hopping model. *AIChE J.* **1981**, *27*, 262−270.

https://doi.org/10.1021/acsomega.3c10441
ACS Omega 2024, 9, 22016−22030

(70) Uhlhorn, R.; Keizer, K.; Burggraaf, A. Gas transport and separation with ceramic membranes. Part II. Synthesis and separation properties of microporous membranes. *J. Membr. Sci.* **1992**, *66*, 271−287.
(71) Auerbach, S. M.; Carrado, K. A.; Dutta, P. K. *Handbook of Zeolite Science and Technology*; CRC Press, 2003.
(72) Sakhaee-Pour, A.; Bryant, S. L. Gas Permeability of Shale. *SPE Reservoir Eval. Eng.* **2012**, *15*, 401−409.
(73) Zhang, W.; Xu, J.; Jiang, R.; Cui, Y.; Qiao, J.; Kang, C.; Lu, Q. Employing a quad-porosity numerical model to analyze the productivity of shale gas reservoir. *J. Pet. Sci. Eng.* **2017**, *157*, 1046−1055.
(74) Ertekin, T.; King, G. R.; Schwerer, F. C. Dynamic gas slippage: a unique dual-mechanism approach to the flow of gas in tight formations. *SPE Form. Eval.* **1986**, *1*, 43−52.
(75) Beskok, A.; Karniadakis, G. E. Report: a model for flows in channels, pipes, and ducts at micro and nano scales. *Microscale Thermophys. Eng.* **1999**, *3*, 43−77.
(76) Liu, S.; Harpalani, S. A new theoretical approach to model sorption-induced coal shrinkage or swelling. *AAPG Bull.* **2013**, *97*, 1033−1049.
(77) Wu, K.; Li, X.; Chen, Z. A model for gas transport through nanopores of shale gas reservoirs. *Acta Pet. Sin.* **2015**, *36*, 837.
(78) Freeman, C. M.; Moridis, G. J.; Blasingame, T. A. A Numerical Study of Microscale Flow Behavior in Tight Gas and Shale Gas Reservoir Systems. *Transp. Porous Media* **2011**, *90*, 253−268.
(79) Javadpour, F.; Fisher, D.; Unsworth, M. Nanoscale gas flow in shale gas Sediments. *J. Can. Pet. Technol.* **2007**, *46*, 55−61.
(80) Randolph, P. L.; Soeder, D. J.; Chowdiah, P. Porosity and Permeability of Tight Sands. In *SPE Unconventional Gas Recovery Symposium*; OnePetro, 1984.
(81) Liu, W.; Lu, P. Research progress on shale gas reservoir characteristics and seepage mechanism. *Petrochem. Ind. Appl.* **2022**, *41*, 9−14.
(82) Du, S.; Shen, W.; Zhao, Y. Quantitative Evaluation Of Stress Sensitivity In Shale Reservoirs: Ideas And Applications. *Chin. J. Theor. Appl. Mech.* **2022**, *54*, 2235−2247.
(83) Edwards, R. W. J.; Doster, F.; Celia, M. A.; Bandilla, K. W. Numerical Modeling of Gas and Water Flow in Shale Gas Formations with a Focus on the Fate of Hydraulic Fracturing Fluid. *Environ. Sci. Technol.* **2017**, *51*, 13779−13787.
(84) He, X.; Lu, B.; He, G.; Ren, J.; Wang, W.; Chen, Z.; Gao, Y.; Fang, D. Production characteristics and optimized development technologies for normal-pressure shale gas in the structurally complex areas of southeastern Chongqing. *Oil Gas Geol.* **2021**, *42*, 224−240.
(85) Guo, W. Analysis of Factors Affecting the Decline Trend of Horizontal Well Production in Shale Gas. *J. Chongqing Univ. Sci. Technol., Nat. Sci. Ed.* **2018**, *20*, 36−39.
(86) Liu, F. Advices for Well Jiaoye XHF, Fuling Shale Gas Field by Analyzing Production Data. *Bull. Geol. Sci. Technol.* **2018**, *37*, 196−201.
(87) Guo, W.; Gao, J.; Li, H.; Kang, L.; Zhang, J.; Liu, G.; Liu, Y. The geological and production characteristics of marine-continental transitional shale gas in China: Taking the example of shale gas from Shanxi Formation in Ordos Basin and Longtan Formation in Sichuan Basin. *Miner. Explor.* **2023**, *14*, 448−458.
(88) Wang, Z.; Wang, Y.; Dong, H.; Wang, X. Production Main Control Factors Analysis and Productivity Prediction for Shale Gas of Horizontal Well. *Well Logging Technol.* **2017**, *41*, 577−582.
(89) Zhao, Y.; Huang, X.; Zhang, L.; Li, S.; Li, X.; Xu, H. Numerical simulation of fractured horizontal wells in transitional shale gas reservoirs based on embedded discrete fracture model optimization. *Nat. Gas Ind.* **2023**, *43*, 116−126.

https://doi.org/10.1021/acsomega.3c10441
ACS Omega 2024, 9, 22016−22030